Large Dzyaloshinskii-Moriya interaction and field-free topological chiral spin states in two-dimensional alkali-based chromium chalcogenides

Peng Li, Qirui Cui, Yonglong Ga, Jinghua Liang, and Hongxin Yang *

Ningbo Institute of Materials Technology and Engineering, Chinese Academy of Sciences, Ningbo 315201, China and Center of Materials Science of Optoelectronics Engineering, University of Chinese Academy of Sciences, Beijing 100049, China

(Received 29 December 2021; revised 16 May 2022; accepted 28 June 2022; published 19 July 2022)

Noncentrosymmetric ferromagnetic systems with large Dzylochinskii-Moriya interaction (DMI) have gained intensive attention for hosting topologically protected solitons such as skyrmions and bimerons. Recently, a series of two-dimensional (2D) Li- and Na-based chromium chalcogenides has been theoretically predicted to be a new family of intrinsic inversion asymmetric ferromagnets. Here, by combining first-principles calculations and atomistic spin model simulations, we unveil that there is very large DMI in these series of 2D alkali-based chromium chalcogenides, which enables a variety of filed-free topological spin textures in these structures. Furthermore, we find robust hole-doping tunable DMI in the $LiCrSe_2$ and $NaCrSe_2$ monolayers. Our finding opens up further possibilities toward 2D materials in spintronic devices.

DOI: 10.1103/PhysRevB.106.024419

I. INTRODUCTION

Topological chiral magnetic structures, such as skyrmions [1–4], bimerons [5–7], and spin spirals [8], etc. have been a hot topic for their promising applications for future spintronic devices with high storage density and energy efficiency [9–11] thanks to their unique static and dynamics properties. The asymmetric Dzyaloshinskii-Moriya interaction (DMI) [12,13] plays the key role in generating and stabilizing these fascinating topological chiral textures. The presence of DMI requires sizable spin-orbit coupling (SOC) and inversion symmetry breaking (ISB) [14–16]. For the last few decades, great efforts have been devoted to heavy metal (HM)/ferromagnet (FM) multilayers [17–21] to maximize the interfacial DMI. Recently, with the emergence of intrinsic two-dimensional (2D) magnetic materials [22–25], the artificially constructed magnets with ISB such as Janus structures [26–29] and 2D van der Waals heterostructures [30–33] can realize sizable DMI to form topological spin textures. More appealingly, the multiferroic 2D magnets CrN, $CrCuP_2Se_6$ [34], and Janus magnet-ferroelectric heterostructures [30,35] offer opportunities of effective electrical control of topological magnetism. Exploration of more 2D magnets with intrinsic ISB and tunable topological magnetism will enrich the 2D spintronics phenomenon and enable potential applications.

The triangular-lattice alkali-based chromium chalcogenides ($ACrX_2$, A = alkali atom; X = S, Se, and Te) are a series of layered compounds with distinct magnetic properties [36–39]. Recent reports [40] demonstrate that six types of 2D ferromagnets ($ACrX_2$, A = Li and Na; X = S, Se, and Te) with a Curie temperature of above 209 K can be cleaved from their corresponding layered bulk counterparts from first-principles calculations. The single layer $ACrX_2$ structures are equivalent to the 1 T phase chromium dichalcogenide monolayer [41] intercalating a layer of alkali atoms (Li or Na) on one side of the chalcogen atoms. Therefore, the inversion symmetry in the $ACrX_2$ structures is broken, and one can expect the presence of sizable DMI in these structures. Moreover, the reversibly cationic redox properties of Li and Na atoms [42] in $ACrX_2$ are appealing for the ion gating methods, which have been proved very efficient to control the Heisenberg exchange and magnetic anisotropy energy (MAE) in various 2D magnets [24,43–45]. Additionally, in the $Pt/Co/HfO_2$ system, ion gating can realize a nonvolatile control of DMI [46].

Here, via carrying out first-principles calculations, we find quite large DMI values in all the 2D $ACrX_2$ structures. Especially, the DMI strength in monolayers with Se and Te is strong enough to stabilize field-free topological magnetic textures, which are confirmed by both micromagnetic simulations and atomistic spin model simulations. Moreover, we examine the hole-doping effect to the magnetic parameters in the $LiCrSe_2$ and $NaCrSe_2$ monolayers, and we find that the DMI strength in these two monolayers can be further strengthened.

II. CALCULATION METHOD

All our first-principles calculations are performed within the VIENNA AB INITIO SIMULATION PACKAGE [47–49]. The electron-core interactions were described by the projector augmented-wave method for the pseudopotentials, and the exchange correlation energy was calculated within the generalized gradient approximation of the Perdew-Burke-Ernzerhof form [50,51]. The cutoff energies for expanding plane wave basis for $LiCrX_2$ and $NaCrX_2$ (X = S, Se, Te) are 650 eV and 400 eV, respectively. A vacuum region is set to 20 Å to prevent the artificial coupling between adjacent periodic images. The convergence criterion of electronic iteration is set to 10^{-7} eV and all structures are relaxed until the Hellmann-Feyman

*Hongxin.Yang@nimte.ac.cn

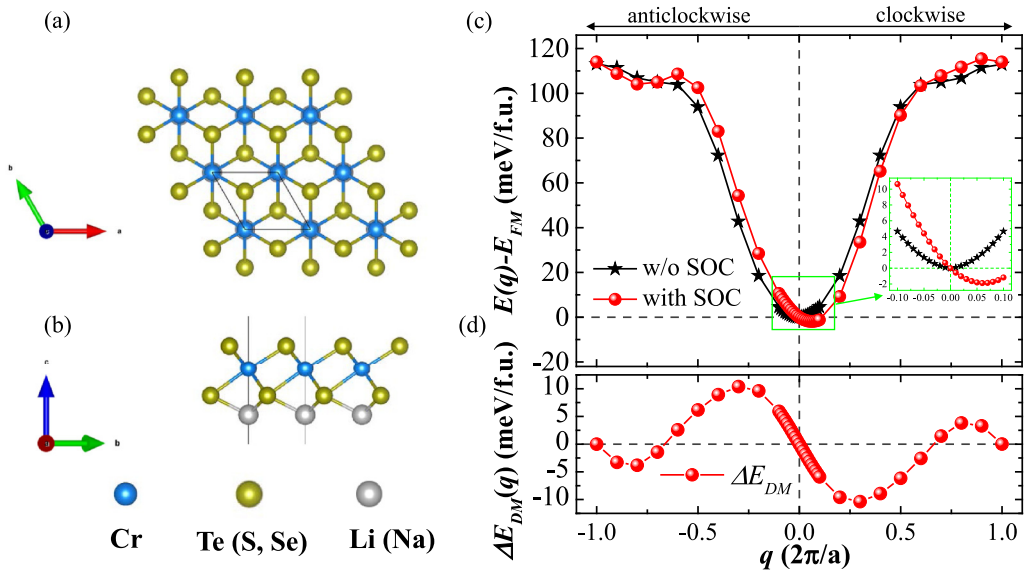

FIG. 1. (a) Top and (b) side views of the crystal structure of a $LiCrTe_2$ monolayers. Calculated spin spiral energy E[q] (c) and DMI energy $\Delta E_{\mathrm{DM}}[q]$ (d) as a function of spiral vector length q along the Γ-K direction. E[q] is given with respect to the ferromagnetic state at q = 0. Red balls and black stars are calculated with and without (w/o) SOC, respectively.

force acting on each atom is less than 0.001 eV/Å. The van der Waals corrections (DFT-D3) [52] were introduced to describe the effect of van der Waals interactions. The GGA + U method is applied ($U_{\mathrm{eff}} = 3.5$ eV) to describe strongly correlated $3d$ electrons of Cr [40]. A Γ centered $24 \times 24 \times 1$ K-point mesh with Monkhorst-Pack scheme was used in the calculations.

III. RESULTS AND DISCUSSION

A. Structural parameters and magnetic anisotropy

The crystal structure of the $ACrX_2$ monolayers is shown in Figs. 1(a) and 1(b). The Cr atoms form a triangular lattice with C_{6v} symmetry, sandwiched by two atomic layers of the same chalcogen atoms S, Se, or Te. One atomic layer of alkali atoms is adjacent to the bottom chalcogen atoms, sitting on top of Cr. The overall symmetry of $ACrX_2$ is C_{3v}. All the relaxed in-plane lattice constant parameters and saturation magnetization M_s are shown in Table I, the optimized lattice constant of Li- and Na-based $ACrX_2$ increases with the radii of chalcogen atoms, which agrees with previous studies [40]. For comparison, we list the lattice constants from previous theoretical works and experiments in Table SI [53]. The calculated magnetic moment of Cr atoms ranges from 3.2 to 3.6 μ_{B}, with an increasing tendency while involving S to Se and Te, for both the $LiCrX_2$ and $NaCrX_2$ series. For convenience, the top chalcogen atoms are labeled as X1 (X = S, Se, Te) and the middle chalcogen atoms are labeled as X2. For all the $ACrX_2$ monolayers, the top chalcogen atoms show larger magnetic moments than the middle chalcogen atoms. Notably, for the top Se and Te atoms, the magnetic moments can reach up to -0.3 μ_{B}.

To investigate the magnetic properties of the $ACrX_2$ monolayers, we adopt the following model Hamiltonian for the Cr atoms:

$$H = -\sum_{i,j} J_{ij}(\mathbf{M}_i \cdot \mathbf{M}_j) - \sum_{i,j} \mathbf{d}_{ij} \cdot (\mathbf{M}_i \times \mathbf{M}_j) - K_{\mathrm{MCA}} \sum_i \left(\mathbf{M}_i^z\right)^2 + E_{\mathrm{ddi}}. \quad (1)$$

In the equations, $\mathbf{M}_i$ and $\mathbf{M}_j$ denote the magnetic moment of each atom at sites i and j. J_{ij}, $\mathbf{d}_{ij}$, K_{MCA} and represent the Heisenberg exchange, DMI, and magnetic anisotropy energy for atoms of sites i and j, respectively.

TABLE I. The calculated lattice constant a, saturation magnetization M_s, DMI parameter D, atomistic DMI parameter d, exchange stiffness A, magnetic anisotropy energy K_{MCA}, magnetic shape anisotropy energy K_{MSA}, and effective magnetic anisotropy K_{eff} per Cr atom, and dimensionless parameter κ for the $ACrX_2$ monolayers.

Structure	a (Å)	M_s (μ_{B})	A (meV Å^2)	D (meV Å)	d (meV)	K_{MCA} (meV)	K_{MSA} (meV)	K_{eff} (meV)	κ
$LiCrS_2$	3.56	2.95	234.37	−2.60	−0.49	0.073	−0.160	−0.087	−4.85
$LiCrSe_2$	3.76	3.00	242.24	−12.56	−2.23	0.008	−0.144	−0.136	−0.34
$LiCrTe_2$	4.08	3.10	191.56	−39.41	−6.44	0.313	−0.123	0.190	0.04
$NaCrS_2$	3.64	2.92	209.13	−2.76	−0.50	0.026	−0.168	−0.142	−6.33
$NaCrSe_2$	3.83	2.98	252.85	−11.16	−1.94	0.211	−0.129	0.082	0.27
$NaCrTe_2$	4.15	3.09	260.13	−31.28	−5.02	1.598	−0.114	1.484	0.64

The magnetic anisotropy energy K_{MCA} is obtained by comparing the energy difference between self-consistent energies while the magnetic axis aligns (100) and (001) orientations. E_{ddi} represents the energy from dipole-dipole interactions, which is described as $E_{\mathrm{ddi}} = \frac{1}{V_{u.c.}}\frac{\mu_0}{2}\sum_{<i,j>}\frac{1}{4\pi r_{ij}^3}[\mathbf{M}_i\cdot\mathbf{M}_j - (\mathbf{M}_i\cdot\mathbf{r}_{ij})(\mathbf{M}_j\cdot\mathbf{r}_{ij})\frac{3}{r_{ij}^2}]$, where r_{ij} is the distance between atoms at site i and j, $\mathbf{r}_{ij}$ represents the vector connecting site i and j, $V_{\mathrm{u.c.}}$ is the unit cell volume. We can estimate E_{ddi} by calculating the magnetic shape anisotropy K_{MSA} in the ferromagnetic configurations [54,55]. The effective anisotropy energy K_{eff} is determined by $K_{\mathrm{eff}} = K_{\mathrm{MCA}} - K_{\mathrm{MSA}}$. As shown in Table I, $LiCrS_2$, $LiCrSe_2$, $NaCrS_2$, and $NaCrSe_2$ display weak perpendicular MAE, which is consistent with previous works [40]. For these monolayers, the shape anisotropy energy K_{MSA} ranges from −0.11 meV/u.c. to −0.17 meV/u.c., which is comparable to the calculated K_{MCA}. From Table I, one can see that the $LiCrS_2$, $NaCrS_2$, and $LiCrSe_2$ monolayers display in-plane effective magnetic anisotropy, whereas for $LiCrTe_2$, $NaCrSe_2$, and $NaCrTe_2$ monolayers, the perpendicular MAE is not compensated by the shape anisotropy energy, and their magnetic easy axis aligns out-of-plane orientation.

B. Dzylochinskii-Moriya interaction

Next, we focus on DMI for the $ACrX_2$ monolayers. Based on the symmetry arguments of Moryia rules [13], the DMI component between two adjacent Cr atoms can be expressed as $\mathbf{d}_{ij} = d_{\parallel}(\widehat{r}_{ij}\times\widehat{z}) + d_z\widehat{z}$, in which $\widehat{r}_{ij}$ is the unit vector between sites i and j, $\widehat{z}$ represents normal to the plane. d_z and $d_{\parallel}$ represent the perpendicular-to-plane and in-plane components of DMI, respectively. The sign of d_z varies for the six nearest neighbors (NNs) of the Cr atom, thus the average value of d_z becomes infinitesimal [26,27]—we will come to this point later.

To elucidate the $d_{\parallel}$ component here, we implement the qSO method which is based on the generalized Bloch theorem. The qSOC method treats the SOC within the first-order perturbation theory and we can calculate the spin spiral energy dispersion in a self-consistent way [34,56,57]. To derive $d_{\parallel}$, we consider the energy dispersion $E[q]$ of homogeneous flat spin spirals in which the magnetic moment of an atom site $\mathbf{R}_i$ is given as $\mathbf{M}_i = M[\sin(\mathbf{q}\cdot\mathbf{r}_i), 0, \cos(\mathbf{q}\cdot\mathbf{r}_i)]$. For ferromagnetic monolayers in the small q region of the vector $\mathbf{q} = (q, 0, 0)$, spiral energy as a function of spiral length q can be expressed as

$$E[q] = Aq^2 + Dq - \frac{K}{2}, \tag{2}$$

where A, D, K are the spin stiffness, DMI parameter, and effective anisotropy, respectively. In this paper, we use the sign convention that $D < 0$ ($D > 0$) signifies a clockwise (anticlockwise) DMI, and $K < 0$ ($K > 0$) implies in-plane (perpendicular) anisotropy. For an atomistic site with $i = 0$, the material parameters A and D can be expressed as a series expansion [58] depending on Heisenberg exchange interactions J_{0j} and y component DMI parameter d_{0j}^y in the atomistic model Eq. (1), respectively, as the following equations:

$$A = \frac{1}{2V}\sum_j J_{0j}\left(r_{0j}^x\right)^2, \tag{3}$$

$$D = \frac{1}{V}\sum_j d_{0j}^y r_{0j}^x. \tag{4}$$

Here, V is the volume of the magnetic part of the unit cell. In this paper, we adopt the atomistic spin model to demonstrate the topological spin configuration for the $ACrX_2$ monolayers.

As a representative example to demonstrate the presence of DMI, we plot the spin spiral energy dispersion with and without SOC for the $LiCrTe_2$ monolayer in Fig. 1(c) . Without SOC, $E[q]$ and $E[-q]$ are symmetric; the spin spiral energy dispersion shows a parabolic behavior with the energy minimum at $q = 0$, indicating a ferromagnetic ground state in the $LiCrTe_2$ monolayer. When SOC is considered, the degeneracy between $E[q]$ and $E[-q]$ is broken and the energy minimum deviates from the ferromagnetic state. From the zoom-in plot of $E[q]$ within the interval between $|q| \leqslant 0.1(\frac{2\pi}{a})$, [see the inset in Fig. 1(c)], we can find that the lowest $E[q]$ locates at $q = 0.06(\frac{2\pi}{a})$, revealing the presence of DMI. The DMI energy reads $\Delta E_{\mathrm{DM}}[q] = (E[q] - E[-q])/2$. From Figs. 1(d) and S1 [53], one can see for the $ACrX_2$ monolayers, $\Delta E_{\mathrm{DM}}[q]$ shows a good sinusoidal behavior, which suggests that we can simplify the atomic Hamiltonian model by considering only the effective NN DMI for $ACrX_2$ monolayers. From Eq. (3), we can derive that $\Delta E_{\mathrm{DM}}[q] \propto Dq$ and $(E[q] - \Delta E_{\mathrm{DM}}[q]) \propto Aq^2$. In the interval between $q = \pm 0.1(\frac{2\pi}{a})$, the DMI energy shows a good linear dependence on q. We can derive the effective DMI parameters between the NN Cr atoms by fitting $E_{\mathrm{DM}}[q]$ from $|q| \leqslant 0.1(\frac{2\pi}{a})$. The exchange stiffness A is obtained by fitting the $E[q]$ of q^2 with the same footing. Additionally, via calculating the SOC-included spin spiral energy in the x-y plane for the $ACrX_2$ monolayers in Fig. S2 [53], we confirm that the d_z components of $ACrX_2$ vanish in the long range.

All the calculated DMI parameters of continuous model D and atomistic model d are shown in Table I. One can see that the light-element-based $LiCrS_2$ and $NaCrS_2$ structures show sizable DMI of −0.49 meV and −0.50 meV, respectively. The DMI magnitude increases drastically as the increasing of chalcogen atomic number. $LiCrSe_2$, and $NaCrSe_2$ monolayers display DMI values of −2.23 meV and −1.94 meV, which are comparable to the DMI reported in Janus structures MnSTe (∼2.63 meV) [26] and CrSeTe (∼2.01 meV) [27] with heavier Te atoms and at some FM/HM interfaces such as the Fe/Ir(111) interface (∼1.7 meV) [18]. For the $LiCrTe_2$ and $NaCrTe_2$ monolayers with the heavier Te atoms, the DMI values reach up to −6.44 meV and −5.02 meV, respectively; those values are comparable to the state-of-art Ir/Fe/Co/Pt multilayers [59] (∼5.5 meV).

From the parameters A, K_{eff}, and D in the continuous model shown in Table I, it is convenient to introduce the dimensionless parameter κ as a criteria to justify the formation of distinct magnetic chiral states, which is described as

$$\kappa = \left(\frac{4}{\pi}\right)^2\frac{AK_{\mathrm{eff}}}{D^2}. \tag{5}$$

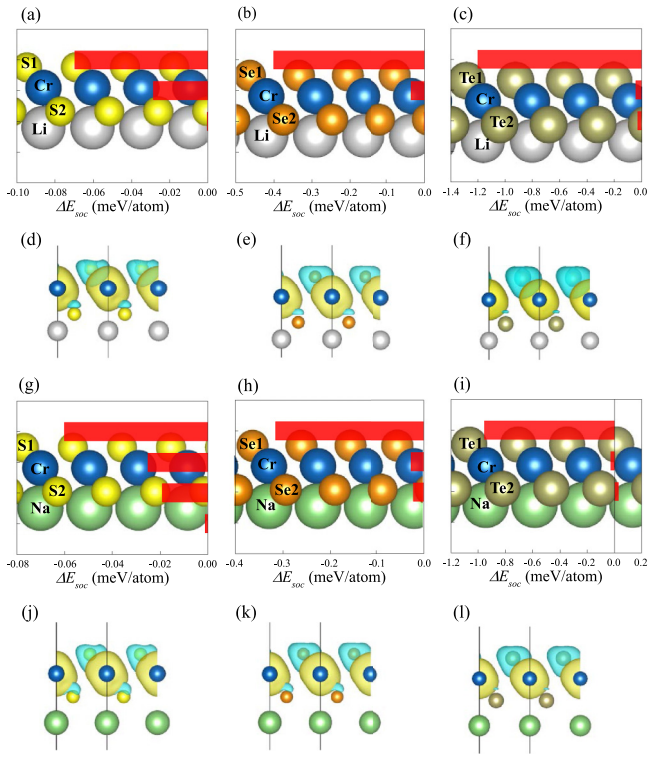

FIG. 2. Atomic-layer-resolved SOC energy of DMI $\Delta E_{\mathrm{DM}}[q]$ at $q = 0.01(\frac{2\pi}{a})$ for (a) $LiCrS_2$, (b) $LiCrSe_2$, (c) $LiCrTe_2$, (g) $NaCrS_2$, (h) $NaCrSe_2$, and (i) $NaCrTe_2$ respectively. Spin density for (d) $LiCrS_2$, (e) $LiCrSe_2$, (f) $LiCrTe_2$, (j) $NaCrS_2$, (k) $NaCrSe_2$, and (l) $NaCrTe_2$, respectively. The yellow and teal regions denote two kinds of spin components, the isosurface is set to 0.005 e/Å^3

For the systems with PMA ($K_{\mathrm{eff}} > 0$) and $0 < \kappa < 1$, indicates spin spiral ground states, and isolated metastable skyrmion can be found in some systems with relatively small κ, e.g., $\kappa = 4.8$ for Fe/W [60]. From Table I, one can see that κ of $LiCrTe_2$, $NaCrSe_2$, and $NaCrTe_2$ show $\kappa < 1$, indicating that the ground state is spin spiral. The $LiCrS_2$, $NaCrS_2$, and $LiCrSe_2$ monolayers show in-plane effective magnetic anisotropy with a negative κ. For $LiCrSe_2$, $|\kappa| < 1$, however, $|\kappa| > 4$ is found in both $LiCrS_2$ and $NaCrS_2$ monolayers with weaker DMI values, which implies that generating topological spin textures in $LiCrS_2$ and $NaCrS_2$ monolayers is difficult. The influence of U_{eff} on the lattice parameter, K_{MCA}, d, and κ are examined, as shown in Fig. S3 [53].

To investigate the origin of large DMI in the $ACrX_2$ monolayers, we explore atomic-layer-resolved SOC energy difference associated to DMI, ΔE_{DM}, for $q = 0.01(2\pi/a)$ as shown in Figs. 2(a)–2(c) and Figs. 2(g)–2(i) for all six $ACrX_2$ structures. It is found that the alkali Li and Na atoms do not contribute to the total DMI for all the structures and the middle chalcogen atoms adjacent to alkali atoms (labeled S_2, Se_2, and Te_2) display weak DMI contribution. In contrast, the top chalcogen atoms (labeled S_1, Se_1, and Te_1) give rise to the largest contribution of ΔE_{DM}, and the ΔE_{DM} increases drastically as the chalcogen atomic number. For these systems, DMI originates mainly from Fert-Lévy mechanism [14,61–63], which is strongly related to the SOC strength of the chalcogen atoms. The respective spin density is presented in Figs. 2(d)–2(f) and Figs. 2(j)–2(l). It is found that the majority spin component is on the Cr atoms, and the density of minority spin component on the top chalcogen atoms is greater than that on the middle chalcogen atoms. With the help of Bader charge analysis [64–67], we find the electron depletion on the alkali atoms Li and Na is around 0.85 e/atom and 0.72 e/atom, respectively. The top chalcogen atoms gain electrons range from 0.51 e/atom to 0.77 e/atom, and the middle chalcogen atoms gain electrons range from 1.13 e/atom to 1.33 e/atom, indicating different band fillings for the top and middle chalcogen atoms. The electronic occupation of magnetic atoms is a key factor for the DMI, as previously reported in the $3d/5d$ interface [68,69] and hydrogen-absorbed Co/graphene interface [70].

The chalcogen p orbitals and the Cr d orbitals are strongly hybridized in the $ACrX_2$ monolayers. For these 2D magnets, both the Heisenberg exchange coupling and DMI originate from the d-p hopping process. To further elucidate how electronic occupation changes the d-p hopping and generates the DMI in the $ACrX_2$ monolayers, we choose the $LiCrSe_2$ as a presentative example. First, we investigate the orbital hybridization-resolved SOC energy matrix elements associated with DMI. We find that only the matrix elements from p_z and p_x orbitals of Se1 atoms contribute significant SOC energy to the total DMI, as shown in Fig. 3(a). Contributions from p orbitals of Se2 atoms and d orbitals of Cr atoms are very small.

Next, we plot the projected density of states in Fig. 3(b). To verify the SOC-affected electronic occupations, we examined the pDOS of $LiCrSe_2$ monolayer including SOC with a nonzero q spiral length of $q = 0.01(\frac{2\pi}{a})$, as shown in Figs. 3(c) and 3(d). Here, only the average value of pDOS on spinor M_z component is plotted, in which positive and negative occupation population numbers indicate the average occupation on each electronic state. Similar to the case of 1 T phase of 2D magnets [71], the Se1, Se2, and Cr atoms form an octahedral crystal structure. For Cr atoms, the spin-up component of the occupied and unoccupied states close to the Fermi level are mainly from the $t_{2g}^{\uparrow}$ bonding states and $e_g^{\uparrow *}$ antibonding states, respectively. The population of occupied electronic states close to the Fermi level for Se1 atoms is larger than that of Se2.

The presence of DMI requires SOC-affected spin-flipping transition from occupied states to unoccupied states [68], which is provided by the hopping between electronic states with different spin components. From the spin components close to the Fermi level in Figs. 3(b)–3(d), the most significant spin-flipping d-p hopping is between occupied Se $p^{\downarrow}$ states to unoccupied states of hybridized Cr d ($e_g^{\uparrow *}$) and Se $p^{\uparrow *}$. To better understand the distinct Fert-Lévy-type DMI contributions [14,61–63] from the top and middle Se atoms, we introduce a toy tight-binding model [72] to describe the SOC affected interorbital scattering in $LiCrSe_2$.

The total DMI from atomic sites i and j can be expressed as the sum of all the interorbital contributions (IO-DMI), $D_{i,j} = \sum_{<m,m'>} D_{ij}^{m,m'}$, where $m(m')$ denote the hybridized electronic states of Se and Cr atoms, respectively. From Moriya's theory [13,73],

$$D_{i,j}^{m,m'} = \frac{4i}{U}[b_{m,m'}C_{m',m} - C_{m,m'}b_{m',m}], \tag{6}$$

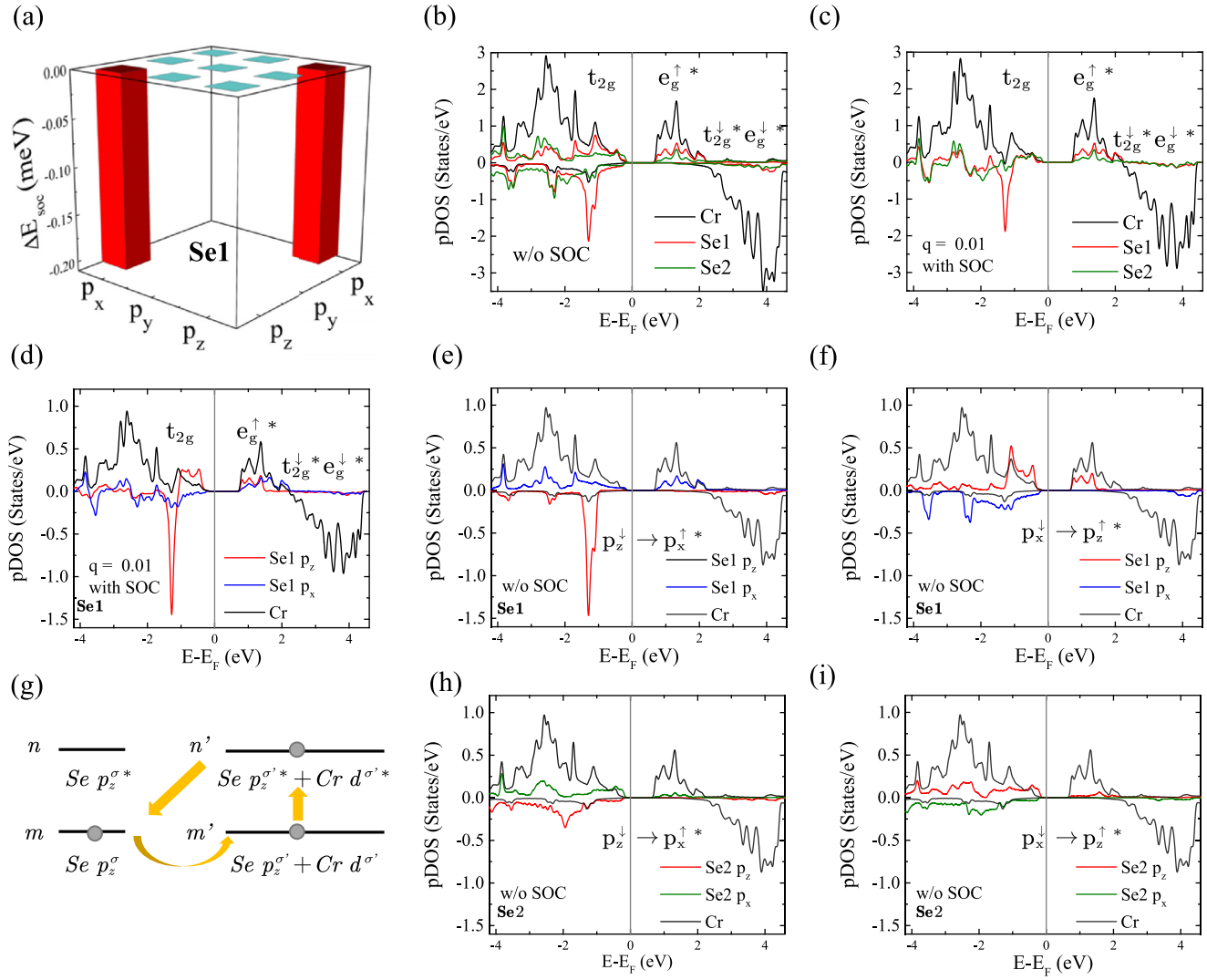

FIG. 3. (a) Orbital hybridization resolved SOC energy matrix elements associated with DMI $\Delta E_{\mathrm{DM}}[q]$ at $q = 0.01(\frac{2\pi}{a})$ for top selenium atoms Se1 in the $LiCrSe_2$ monolayer. (b) The projected density of states (pDOS) without SOC for $LiCrSe_2$ monolayer plotted from contributions of Cr, Se1, and Se2 atoms. (c), (d) pDOS for $LiCrSe_2$ monolayer in qSO calculation when spiral length q is set to $0.01(\frac{2\pi}{a})$, where (c) is plotted from contributions of Cr, Se1, and Se2 atoms, (d) is from contributions of selected p orbitals of Se1 and the total d orbitals of Cr, respectively. (e), (f) The pDOS withou SOC for selected p orbitals of Se1 and the total d orbitals of Cr. (g) Visualization of the toy tight-binding model to explain the DMI contribution from the d-p hopping between Se and Cr atoms, σ and τ denote different spin components. (h), (i) The pDOS withou SOC for selected p orbitals of Se1 and the total d orbitals of Cr. In the pDOS (d)–(f) and (h), (i),the occupation of Cr d orbitals is divided by 3, for a better view.

where $b_{m,m'}$ and $b_{m',m}$ represent the non-SOC hopping integrals between ground states m and m' at sites i and j, respectively. $C_{m,m'}$ and $C_{m',m}$ indicate the indirect hopping between m and m' through the respective excited states n and n', which are described as

$$C_{m,m'} = \frac{\xi}{2} \cdot \left[b_{n',m} \frac{L^*_{m'n'}}{\epsilon_{n'} - \epsilon_{m'}} - b_{m',n} \frac{L_{mn}}{\epsilon_n - \epsilon_m} \right] + c_{m,m'} \quad (7)$$

$$C_{m',m} = \frac{\xi}{2} \cdot \left[b_{n',m} \frac{L^*_{mn}}{\epsilon_n - \epsilon_m} - b_{m',n} \frac{L_{m'n'}}{\epsilon_{n'} - \epsilon_{m'}} \right] + c_{m',m} \quad (8)$$

In Eqs. (7) and (8), ξ represents the SOC strength, L_{mn} denotes the matrix elements of orbital angular momentum of atoms. $\epsilon_m - \epsilon_n$ is the energy difference between ground state and excited state. The terms $b_{n',m}$ and $b_{m',n}$ are the hopping integrals between ground states m, m' and excited states n, n', respectively. $c_{m,m'}$ and $c_{m',m}$ are the SOC-induced hopping between ground states m and m', which are usually very weak. The IO-DMI contributions can be schematized as Fig. 3(g), in which m and n represent the occupied and unoccupied states from Se p orbitals with spin component σ close to the Fermi level, respectively. m' and n' indicate the occupied and unoccupied states between hybridized Se and Cr d orbitals with the opposite spin component τ.

As shown in Figs. 3(e), 3(f), 3(h), and 3(i), for both the top and middle Se atoms Se1 and Se2, the unoccupied states of $p^{\downarrow}$ orbitals are far from the Fermi level, thus hopping terms between Se $p^{\downarrow}$ to hybridized Cr d and Se $p^{\uparrow *}$ consist of two competing contributions, namely, the hopping between

Se $p_z^{\downarrow}$ to hybridized Cr d and Se $p_x^{\uparrow *}$ ($p_z^{\downarrow} \rightarrow p_x^{\uparrow *}$), and the hopping between Se $p_x^{\downarrow}$ to Cr d and Se $p_z^{\uparrow *}$ ($p_x^{\downarrow} \rightarrow p_z^{\uparrow *}$). From Figs. 3(d)–3(f), Se1 atoms provide a heavily populated $p_z^{\downarrow}$ state, which indicates distinct d-p hopping process from the Cr-Se1 and the Cr-Se2 bonds. With the help of the aforementioned toy tight-binding model, we can analyze the IO-DMI contributions from Cr-Se1 and Cr-Se2.

For the hopping term $p_z^{\downarrow} \rightarrow p_x^{\uparrow *}$ from both Cr-Se1, one can see in Figs. 3(b)–3(d), the unoccupied states of the Se1 $p_z{}^{\downarrow}$ orbital is far from the Fermi level, thus the hopping magnitude from states m to n and from m' to n can be negligible. Therefore, one can get a nonzero value from the hopping integral $b_{n',m}$ and an infinitesimal value of $b_{m',n}$. By consequence, we have $C_{m'n} = C_{n'm}^{*}$. Since $b_{m,m'} = b_{m',m}$, the term $b_{m,m'}C_{m',m} - C_{m,m'}b_{m',m}$ is imaginary. From Eq. (6), one can find sizable IO-DMI $D_{i,j}^{m,m'}$ for the hopping from Se1 $p_z^{\downarrow}$ to hybridized Cr d and Se1 $p_x^{\uparrow *}$ states.

From similar analysis, we can find nonzero IO-DMI contributions of hopping $p_x^{\downarrow} \rightarrow p_z^{\uparrow *}$ of Cr-Se1 and the competing hopping terms from Cr-Se2. From the selected pDOS in Figs. 3(c)–3(f), the occupation population of Se1 $p_z^{\downarrow}$ orbital is much larger than that of Se1 $p_x^{\downarrow}$, leading to greater integrals $b_{n',m}$, $b_{m,m'}$ from $p_z^{\downarrow} \rightarrow p_x^{\uparrow *}$ for Se1. Therefore, the IO-DMI contributed by the hopping from Se1 $p_z^{\downarrow} \rightarrow p_x^{\uparrow *}$ of dominants. For Se2, the occupation population of $p_z^{\downarrow}$ is close to that of $p_x^{\downarrow}$, and so are $p_x^{\uparrow *}$ and $p_z^{\uparrow *}$. Thus, the integrals $b_{n',m}$, $b_{m,m'}$ from Se2 $p_x^{\downarrow} \rightarrow p_z^{\uparrow *}$ are close to that from Se2 $p_z^{\downarrow} \rightarrow p_x^{\uparrow *}$. As a result, the competing IO-DMI contributions in Se2 compensate each other. As a consequence, the DMI contributions in $LiCrSe_2$ are mainly contributed by the hopping between Se1 $p_z{}^{\downarrow}$ to hybridized Cr d and Se1 $p_x^{\uparrow *}$ orbitals.

To conclude, in the $LiCrSe_2$ monolayers, the distinct d-p hopping process in the top and middle chalcogen atoms is due to their different band fillings. More specifically, the hopping between $p_z{}^{\downarrow}$ states of top Se1 atoms and hybridized Se1 $p_x{}^{\uparrow}$–Cr $d^{\uparrow}$ states is responsible for the significant DMI.

C. Heisenberg exchange interactions and exchange stiffness

The calculated parameters of exchange stiffness A are listed in Table I. From these results, one can see from $NaCrS_2$, $NaCrSe_2$, and $NaCrTe_2$, the exchange stiffness A increases with the chalcogen atomic number. Interestingly, $LiCrTe_2$ display a weaker A compared to the $LiCrSe_2$ and $LiCrS_2$ monolayers. However, previous works [40] considered only the NN Heisenberg exchange J_1, showing that J_1 increases with the chalcogen atomic number for both the Li- and Na-based $ACrX_2$ monolayers. Experimental research demonstrates that the bulk compound of $LiCrTe_2$ favors a helical spin structure due to further neighbor antiferromagnetic interactions [38]. Thus, we refer to the beyond NN interactions for the $ACrX_2$ monolayers.

First, we derive the NN, the next-nearest neighbor (NNN), and the third-nearest-neighbor (NNNN) Heisenberg interactions for the $ACrX_2$ monolayers by comparing the energy of four different magnetic configurations in Fig. S4 [53,74]. The results are shown in Table II, labeled J_1, J_2, and J_3. It is found that the FM J_1 gradually increases while evolving S to Se and Te. All six $ACrX_2$ monolayers show weak FM NNN exchange J_2. The NNNN exchange J_3 for all six structures are antiferromagnetic (AFM). Interestingly, the frustration from the NNNN AFM exchange interaction J_3 and the frustration ratio J_3/J_1 also increase as the chalcogen atomic number.

TABLE II. The NN, NNN, NNNN Heisenberg exchanges J_1, J_2, and J_3, the frustration ratio J_3/J_1, the effective exchange stiffness A_{eff} derived from J_1, J_2, and J_3, and the ratio between DMI strength d and NN Heisenberg exchange J_1 for the $ACrX_2$ monolayers. Here, J_1, J_2, and J_3 are deduced by comparing the energy of different magnetic configurations.

Structure	J_1	J_2	J_3	J_3/J_1	A_{eff}	$\lvert d\rvert/J_1$
$LiCrS_2$	22.60	0.85	−1.42	−0.06	182.48	0.02
$LiCrSe_2$	25.33	1.13	−3.12	−0.12	170.00	0.09
$LiCrTe_2$	26.76	1.73	−6.72	−0.25	80.85	0.24
$NaCrS_2$	21.40	0.48	−1.54	−0.07	165.62	0.02
$NaCrSe_2$	24.06	1.01	−2.72	−0.11	181.00	0.08
$NaCrTe_2$	27.18	1.64	−5.70	−0.21	133.93	0.18

For a hexagonal lattice with the q vector propagating along the Γ-K direction of the reciprocal space, the energy dispersion relation for exchange interactions up to NNNN can be described as [75–77]

$$E_{\text{SS}}[q] = -[\cos(2\pi q) + 2\cos(\pi q)]J_1 - [1 + 2\cos(3\pi q)]J_2 - [\cos(4\pi q) + 2\cos(2\pi q)]J_3. \quad (9)$$

To verify the influence of the NNNN AFM exchange on the behavior of exchange stiffness for the $ACrX_2$, we calculated the spin spiral energy dispersion $E_{\text{SS}}[q]$ by substituting J_1, J_2, and J_3 into Eq. (9). Next, we compare $E_{\text{SS}}[q]$ and $E[q] - \Delta E_{\text{DM}}[q]$, where $E[q] - \Delta E_{\text{DM}}[q]$ is the SOC affected spin spiral energy excluding the DMI contribution. The results for $ACrX_2$ with Se and Te are shown in Figs. 4(a)–4(d). The behavior of $E_{\text{SS}}[q]$ is similar to that of $E[q] - \Delta E_{\text{DM}}[q]$, where

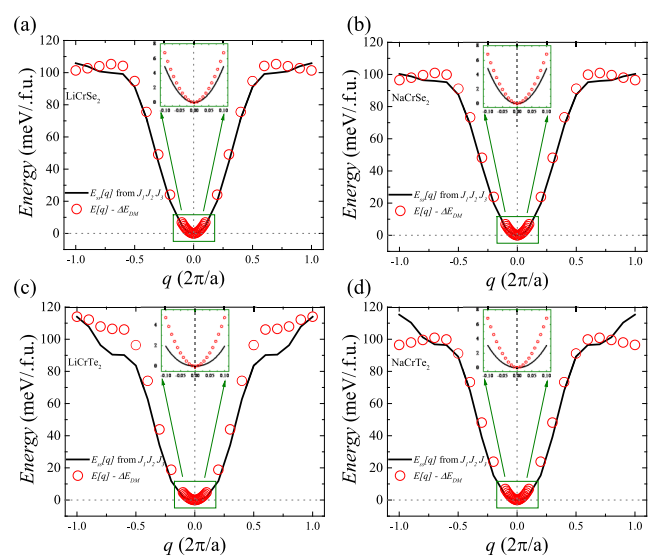

FIG. 4. For (a) $LiCrSe_2$, (b) $NaCrSe_2$, (c) LiCrTe, and (d) $NaCrTe_2$, the red circles represent $E[q] - \Delta E_{\text{DM}}[q]$, the black curves are derived from substituting J_1, J_2, and J_3 into Eq. (9), respectively.

TABLE III. The NN, NNN, NNNN Heisenberg exchange J_1^*, J_2^*, and J_3^* in meV, the ratio of J_3^*/J_1^*, and the ratio between DMI strength d and NN Heisenberg exchange J_1^* for the $ACrX_2$ monolayers, J_1^*, J_2^*, and J_3^* are obtained from fitting the results of $E[q] - \Delta E_{DM}[q]$.

Structure	J_1^*	J_2^*	J_3^*	J_3^*/J_1^*	$\lvert d\rvert/J_1^*$
$LiCrS_2$	21.47	0.51	0.12	0.005	0.02
$LiCrSe_2$	24.81	0.63	−1.34	−0.05	0.09
$LiCrTe_2$	27.78	0.78	−4.06	−0.15	0.23
$NaCrS_2$	20.39	0.32	−0.08	−0.004	0.02
$NaCrSe_2$	23.49	0.73	−1.00	−0.04	0.08
$NaCrTe_2$	27.77	0.97	−3.21	−0.12	0.18

the AFM J_3 is not strong enough to change the FM ground state for the $ACrX_2$ monolayers. From the zoom-in plot of $E_{SS}[q]$ with $|q| \leqslant 0.1(\frac{2\pi}{a})$ [see the inset in the upper part of Figs. 4(a)–4(d)], the effective spin stiffness A_{eff} can be derived by fitting $E_{SS}[q]$ of q^2, which are listed in Table II. The values of A_{eff} are much smaller than the respective A in Table I for all the $ACrX_2$ monolayers.

To explain the discrepancy here, we deduce the effective NN, NNN, and NNNN Heisenberg exchange interactions for the $ACrX_2$ monolayers via fitting $E[q] - \Delta E_{DM}[q]$ by Eq. (9). The calculated J_1^*, J_2^*, and J_3^* are shown in Table III. From Table III, all six $ACrX_2$ monolayers exhibit strong FM NN exchange coupling J_1^* and weak NNN FM exchange J_2^*, which agrees the behavior of J_1 and J_2 in Table II. However, it is found that a significant discrepancy exists between the values of J_3^* and J_3.

To examine the impact from SOC effect here, we derive the effective NN, NNN, and NNNN Heisenberg exchange interactions from fitting non-SOC $E[q]$ in Fig. 1(c) for $LiCrTe_2$, the obtained values of NN, NNN, and NNNN exchange interactions read $J_1^{**} = 27.53$ meV, $J_2^{**} = 0.81$ meV, $J_3^{**} = -4.22$ meV, which are close to the values of J_1^*, J_2^*, and J_3^* for $LiCrTe_2$. Therefore, the difference between J_3 and J_3^* cannot be attributed to the SOC effect. Note that J_1^*, J_2^*, and J_3^* contain the contributions from higher-order interactions (HOIs) [75,78]l more specifically, J_3^* consists of the contributions of NNNN Heisenberg exchange interaction and the higher-order biquadratic exchange interaction [75,78,79]. As a representative example, we calculated the biquadratic interaction B for $LiCrTe_2$, which reads $B = 2.70$ meV, the calculation details are given in the Supplemental Material [53]. For $LiCrTe_2$ monolayer, we substitute the values J_1, J_2, and $J_3 + B$ [see the values for $LiCrTe_2$ in Table II] into Eq. (9) and derive the effective exchange stiffness. The obtained value reads $A'_{eff} = 203.58$ meV, which is consistent with the respective values in Table I. To sum up, for $LiCrTe_2$, the biquadratic interaction B exhibits a significant effect on exchange stiffness A obtained from spin spiral calculations.

A similar phenomenon can be found in $NiX_2(X =$ Cl, Br, and I) systems [77], where the biquadratic interaction can compensate the frustration from NNNN AFM interaction. Particularly, in a $NiCl_2$ monolayer, the frustration ratios J_3/J_1 reache up to −0.3, the biquadratic interaction compensates the NNNN AFM exchange, and stabilizes the FM ground state for $NiCl_2$ [77,80]. For the $ACrX_2$ monolayers, the biquadratic interaction can decrease the effective frustration ratios (see J_3/J_1 in Table II and J_3^*/J_1^* in Table III), thereby increasing the exchange stiffness.

The $ACrX_2$ monolayers show strong NN FM exchange and large DMI values. More appealingly, from the ratios $|d|/J_1$ in Table II and $|d|/J_1^*$ in Table III, the structures with Se and Te can host topological chiral textures. By considering the beyond-NN interactions, one can more accurately study the dynamic properties of topological solitons. However, to explore the dynamic behavior of skyrmions, the HOIs other than biquadratic interaction also need to be considered [75], which is beyond the scope of our paper. For static models in micromagnetic simulations and atomistic spin model simulations, we adopt approximate models by considering only the NN interactions for all the $ACrX_2$ monolayers.

D. Hole doping tuning magnetic interactions in the $NaCrSe_2$ and $LiCrSe_2$ monolayer

The alkali atoms Li and Na are often used in batteries due to their reversibly cationic redox properties [42]. For $ACrX_2$ monolayers, the redox of Li or Na cations can be regarded as a hole-doping process. Here, we choose $LiCrSe_2$ and $NaCrSe_2$ to investigate the hole-doping effect on the magnetic properties. The hole concentration ranges from 0.05 to 0.30 hole per unit cell (hole/u.c.). It is shown in Fig. 5(a), the DMI strength for both $LiCrSe_2$ and $NaCrSe_2$ gradually increases with the hole concentration increasing, and the hole doping affects $NaCrSe_2$ greater than $LiCrSe_2$. The DMI value of pristine $NaCrSe_2$ is smaller than that of pristine $LiCrSe_2$, however, while doping concentration is larger than 0.20 hole/u.c., the DMI value of $NaCrSe_2$ exceeds that of $LiCrSe_2$. For both $LiCrSe_2$ and $NaCrSe_2$, the DMI value reaches a peak with 0.25 hole/u.c. The calculated magnetic anisotropy in Fig. 5(b) shows a nonmonotonic behavior against doping concentration for both $LiCrSe_2$ and $NaCrSe_2$. Particularly, while the hole concentration is larger than 0.15 hole/u.c., the $NaCrSe_2$ monolayer exhibits strong in-plane magnetic anisotropy.

The NN, NNN, and NNNN Heisenberg exchange interactions are shown in Fig. 5(c). For both $LiCrSe_2$ and $NaCrSe_2$, the NN ferromagnetic exchange interaction J_1 gradually increases as the hole concentration increases, while the variation from beyond-NN interactions J_2 and J_3 is relatively small. In Fig. 5(d), we plot the exchange stiffness A for $NaCrSe_2$ and $LiCrSe_2$ monolayers with different hole concentrations. For the cases with hole concentrations greater than 0.05 hole/u.c., the exchange stiffness A increases as the increasing doping concentration for both $NaCrSe_2$ and $LiCrSe_2$.

To investigate the microscopic origin of DMI varying with hole concentration, we plot the atomic-layer-resolved SOC energy of DMI with $\Delta E_{DM}[q] = 0.01(2\pi/a)$ under different hole concentrations in Figs. 5(e) and 5(f) for $LiCrSe_2$ and $NaCrSe_2$, respectively. As one can see, the clockwise DMIs for doped $LiCrSe_2$ and $NaCrSe_2$ are determined by the contribution from the top selenium atoms Se1. Interestingly, while the hole concentration is larger than 0.10 hole/u.c., the middle selenium atoms Se2 in $NaCrSe_2$ give rise to an anticlockwise DMI contribution with an increasing trend against the hole concentration. However, the clockwise DMI contribution

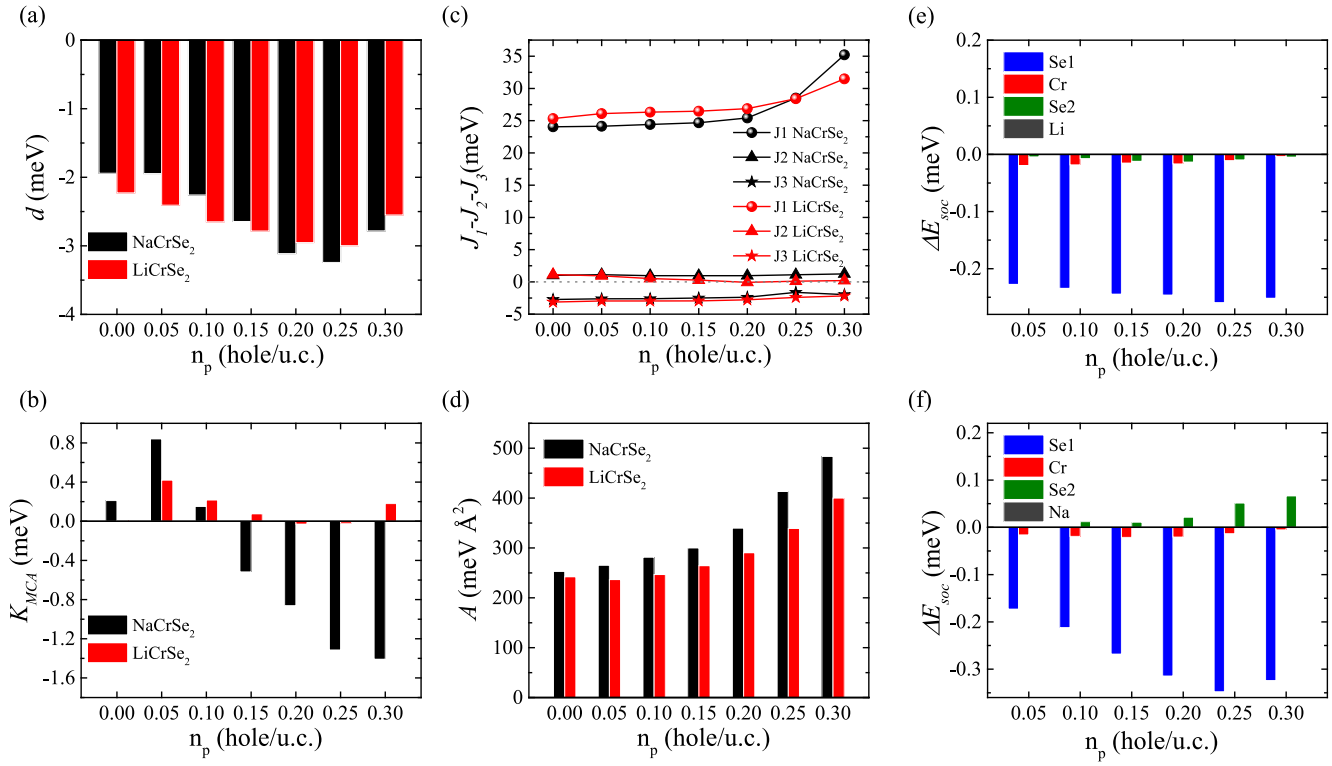

FIG. 5. The calculated (a) DMI strength d, (b) magnetic anisotropy K_{MCA}, (c) Heisenberg exchange J_1, J_2, and J_3 vary with the hole doping concentration for $NaCrSe_2$ and $LiCrSe_2$ monolayers, respectively. (d) The exchange stiffness A for $NaCrSe_2$ and $LiCrSe_2$ monolayers under different hole doping concentrations. The atomic-layer-resolved SOC energy for DMI $\Delta E_{SOC}[q]$ at $q = 0.01(\frac{2\pi}{a})$ for (e) $LiCrSe_2$ and (f) $NaCrSe_2$ monolayers varying with hole concentration, respectively.

from Se1 is far more significant; for instance, $NaCrSe_2$ under various hole concentrations exhibits clockwise DMI.

E. Micromagnetic simulations

With exchange stiffness A, DMI parameter D and MAE K_{MCA} listed in Table I, we perform the micromagnetic simulations with the Mumax[3] package [81]. The magnetization dynamics of the ith magnetic unit cell $\mathbf{M}_i$ can be described by the Landau-Lifshitz-Gilbert equation:

$$\frac{d\mathbf{M}_i}{dt} = -\gamma \mathbf{M}_i \times \mathbf{H}_i + \frac{\alpha}{M_s}\mathbf{M}_i \times \frac{d\mathbf{M}_i}{dt}. \tag{10}$$

Here, γ and α denote the gyromagnetic ratio and damping constant, respectively. $\mathbf{H}_i$ is the effective field for the ith unit cell, M_s denotes the saturation magnetization. The $ACrX_2$ monolayers are modeled in 80 nm × 80 nm areas with periodic boundary conditions. The mash size is set to 0.4 nm × 0.4 nm. Note that for all $ACrX_2$ monolayers, nonzero magnetic moments can be found in Cr and chalcogen atoms, so we take the thickness to be $t = 0.3$ nm, which is approximately the distance between top and bottom chalcogen atoms along the c axis. The Gilbert damping constant α is set to 0.1 and the demagnetization field is considered in the simulations [82,83].

The relaxed magnetization configurations for the $ACrX_2$ monolayers are shown in Figs. 6(a)–6(d). One can see that $ACrX_2$ monolayers with Se and Te can host field-free topological spin textures. Labyrinth domains are found in $LiCrSe_2$, while the coexistent Néel-type skyrmions and labyrinth domains can be stabilized in other $ACrX_2$ monolayers. Interestingly, the density of skyrmions increases with the sequence of $NaCrSe_2$, $NaCrTe_2$, and $LiCrTe_2$, whose DMIs are shown in Table I. However, the DMI magnitude of $LiCrS_2$ and $NaCrS_2$ monolayers is not strong enough to support

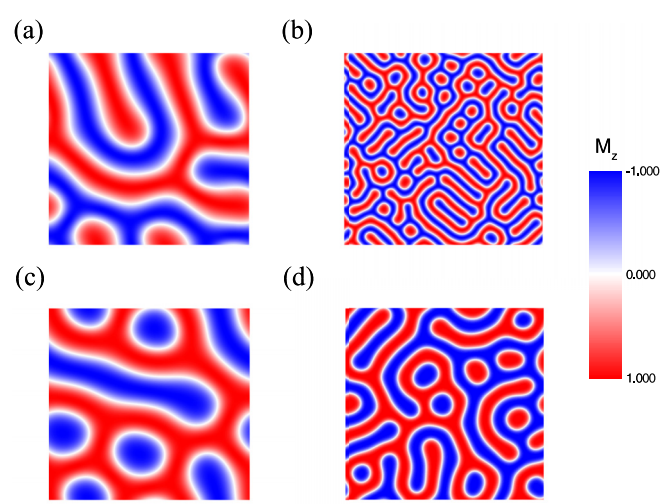

FIG. 6. The relaxed chiral magnetization configuration in a periodical nanodisk of 80 nm × 80 nm in the absence of external field for (a) $LiCrSe_2$, (b) $LiCrTe_2$, (c) $NaCrSe_2$, and (d) $NaCrTe_2$ monolayers, respectively. The color map indicates the out-of-plane spin component of Cr atoms.

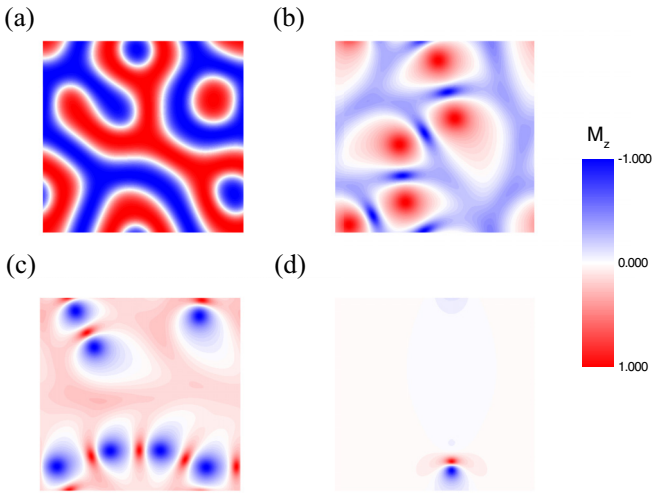

FIG. 7. The relaxed chiral magnetization configuration in a periodical nanodisk of 80 nm × 80 nm in the absence of external field for $NaCrSe_2$ monolayer with hole concentration of (a) 0.1 hole/u.c., (b) 0.15 hole/u.c., (c) 0.2 hole/u.c., and (d) 0.25 hole/u.c., respectively. The color map indicates the out-of-plane spin component of Cr atoms.

topological magnetism, thus one can only find ferromagnetic domains in these two structures.

The magnetic parameters of the $NaCrSe_2$ monolayer are more sensitive against hole doping than that of the $LiCrSe_2$ monolayer; the relaxed magnetization configurations for $NaCrSe_2$ under various hole concentrations are shown in Figs. 7(a)–7(d). $NaCrSe_2$ with hole concentration of 0.1 per unit cell shows perpendicular magnetic anisotropy and can host coexistent Néel-type skyrmions and labyrinth domains. From Figs. 5(b)–5(d), for $NaCrSe_2$ with hole concentrations of 0.15, 0.2, 0.25, and 0.3 per unit cell, both the magnitude of in-plane anisotropy energy K_{MCA} and exchange stiffness A increase with the increasing hole concentration. Loops of vortex and antivortex, Néel-type bimerons chains and isolated Néel-type bimerons can be found in $NaCrSe_2$ with hole concentrations of 0.15, 0.2, and 0.25 per unit cell, respectively. However, in the case with largest out-of-plane magnetic anisotropy with 0.05 hole/u.c. and the case with strongest in-plane effective magnetic anisotropy with 0.3 hole/u.c., field-free topological spin textures cannot be stabilized.

For comparisons, the atomistic spin model simulations for $ACrX_2$ monolayers are performed with the Vampire package [84], shown in Figs. S6 and S7 [53]. The results from micromagnetic simulations and atomistic spin model simulations for $ACrX_2$ monolayers agree with each other.

IV. CONCLUSION

We have performed first-principles calculations and atomistic spin model simulations to demonstrate the presence of large DMI in 2D alkali-based chromium chalcogenides. The DMI in these $ACrX_2$, (A = Li or Na, X = S, Se, Te) monolayers originates mainly from the top chalcogen atoms in the slabs. The middle chalcogen atoms in the slabs, however, contribute almost negligible SOC energy associated with DMI. The distinct contribution of DMI is due to different electronic occupation patterns for the top and middle chalcogen atoms, which strongly impact the SOC-affected d-p hopping process. Furthermore, we find that the hole doping can effectively enhance the DMI values for both $LiCrSe_2$ and $NaCrSe_2$ monolayers. From the atomistic spin model simulations, we find all $ACrX_2$ monolayers with Se and Te atoms can stabilize various field-free topological spin textures, and by adjusting the hole doping concentrations, we can effectively control the chiral spin structures in the $NaCrSe_2$ monolayer. Altogether, our paper suggests a series of topological spin texture hosting 2D FMs with possible electrochemical tunability.

ACKNOWLEDGMENTS

This work was supported by National Natural Science Foundation of China (Grants No. 11874059 and No. 12174405), Key Research Program of Frontier Sciences, CAS (Grant No. ZDBS-LY-7021), Ningbo Key Scientific and Technological Project (Grant No. 2021000215), Pioneer and Leading Goose R&D Program of Zhejiang Province under Grant No. 2022C01053, Zhejiang Provincial Natural Science Foundation (Grant No. LR19A040002), and Beijing National Laboratory for Condensed Matter Physics (Grant No. 2021000123).

[1] A. Fert, N. Reyren, and V. Cros, Magnetic skyrmions: Advances in physics and potential applications, Nat. Rev. Mater. **2**, 17031 (2017).

[2] X. Z. Yu, Y. Onose, N. Kanazawa, J. H. Park, J. H. Han, Y. Matsui, N. Nagaosa, and Y. Tokura, Real-space observation of a two-dimensional skyrmion crystal, Nature (London) **465**, 901 (2010).

[3] R. Wiesendanger, Nanoscale magnetic skyrmions in metallic films and multilayers: A new twist for spintronics, Nat. Rev. Mater. **1**, 16044 (2016).

[4] W. Legrand, D. Maccariello, F. Ajejas, S. Collin, A. Vecchiola, K. Bouzehouane, N. Reyren, V. Cros, and A. Fert, Room-temperature stabilization of antiferromagnetic skyrmions in synthetic antiferromagnets, Nat. Mater. **19**, 34 (2020).

[5] N. Gao, S.-G. Je, M.-Y. Im, J. W. Choi, M. Yang, Q. Li, T. Y. Wang, S. Lee, H.-S. Han, K.-S. Lee, W. Chao, C. Hwang, J. Li, and Z. Q. Qiu, Creation and annihilation of topological meron pairs in in-plane magnetized films, Nat. Commun. **10**, 5603 (2019).

[6] K.-W. Moon, J. Yoon, C. Kim, and C. Hwang, existence of In-Plane Magnetic Skyrmion and Its Motion Under Current Flow, Phys. Rev. Applied **12**, 064054 (2019).

[7] X. Li, L. Shen, Y. Bai, J. Wang, X. Zhang, J. Xia, M. Ezawa, O. A. Tretiakov, X. Xu, and M. Mruczkiewicz, Bimeron clusters in chiral antiferromagnets, npj Comput. Mater. **6**, 169 (2020).

[8] M. Bode, M. Heide, K. von Bergmann, P. Ferriani, S. Heinze, G. Bihlmayer, A. Kubetzka, O. Pietzsch, S. Blügel, and R. Wiesendanger, Chiral magnetic order at surfaces driven by inversion asymmetry, Nature (London) **447**, 190 (2007).

[9] J. Sampaio, V. Cros, S. Rohart, A. Thiaville, and A. Fert, Nucleation, Stability and current-induced motion of isolated magnetic skyrmions in nanostructures, Nat. Nanotechnol. **8**, 839 (2013).

[10] K. M. Song, J.-S. Jeong, B. Pan, X. Zhang, J. Xia, S. Cha, T.-E. Park, K. Kim, S. Finizio, J. Raabe, J. Chang, Y. Zhou, W. Zhao, W. Kang, H. Ju, and S. Woo, Skyrmion-based artificial synapses for neuromorphic computing, Nat. Electron. **3**, 148 (2020).

[11] X. Zhang, Y. Zhou, K. Mee Song, T.-E. Park, J. Xia, M. Ezawa, X. Liu, W. Zhao, G. Zhao, and S. Woo, Skyrmion-electronics: Writing, deleting, reading and processing magnetic skyrmions toward spintronic applications, J. Phys.: Condens. Matter **32**, 143001 (2020).

[12] I. Dzyaloshinsky, A thermodynamic theory of "weak" ferromagnetism of antiferromagnetics, J. Phys. Chem. Solids **4**, 241 (1958).

[13] T. Moriya, Anisotropic superexchange interaction and weak ferromagnetism, Phys. Rev. **120**, 91 (1960).

[14] A. Fert and P. M. Levy, Role of Anisotropic Exchange Interactions in Determining the Properties of Spin-Glasses, Phys. Rev. Lett. **44**, 1538 (1980).

[15] H. Yang, A. Thiaville, S. Rohart, A. Fert, and M. Chshiev, Anatomy of Dzyaloshinskii-Moriya Interaction at Co/Pt Interfaces, Phys. Rev. Lett. **115**, 267210 (2015).

[16] H. Yang, G. Chen, A. A. C. Cotta, A. T. N'Diaye, S. A. Nikolaev, E. A. Soares, W. A. A. Macedo, K. Liu, A. K. Schmid, A. Fert, and M. Chshiev, Significant Dzyaloshinskii-Moriya interaction at graphene-ferromagnet interfaces due to the Rashba effect, Nat. Mater. **17**, 605 (2018).

[17] S. Heinze, K. Von Bergmann, M. Menzel, J. Brede, A. Kubetzka, R. Wiesendanger, G. Bihlmayer, and S. Blügel, Spontaneous atomic-scale magnetic skyrmion lattice in two dimensions, Nat. Phys. **7**, 713 (2011).

[18] B. Dupé, M. Hoffmann, C. Paillard, and S. Heinze, Tailoring magnetic skyrmions in ultra-thin transition metal films, Nat. Commun. **5**, 4030 (2014).

[19] O. Boulle, J. Vogel, H. Yang, S. Pizzini, D. de Souza Chaves, A. Locatelli, T. O. Menteş, A. Sala, L. D. Buda-Prejbeanu, and O. Klein, Room-temperature chiral magnetic skyrmions in ultrathin magnetic nanostructures, Nat. Nanotechnol. **11**, 449 (2016).

[20] A. Soumyanarayanan, M. Raju, A. G. Oyarce, A. K. Tan, M.-Y. Im, A. Petrović, P. Ho, K. Khoo, M. Tran, and C. Gan, Tunable room-temperature magnetic skyrmions in Ir/Fe/Co/Pt multilayers, Nat. Mater. **16**, 898 (2017).

[21] M. Raju, A. Yagil, A. Soumyanarayanan, A. K. Tan, A. Almoalem, F. Ma, O. Auslaender, and C. Panagopoulos, The evolution of skyrmions in Ir/Fe/Co/Pt multilayers and their topological Hall signature, Nat. Commun. **10**, 696 (2019).

[22] B. Huang, G. Clark, E. Navarro-Moratalla, D. R. Klein, R. Cheng, K. L. Seyler, D. Zhong, E. Schmidgall, M. A. McGuire, and D. H. Cobden, Layer-dependent ferromagnetism in a van der Waals crystal down to the monolayer limit, Nature (London) **546**, 270 (2017).

[23] C. Gong, L. Li, Z. Li, H. Ji, A. Stern, Y. Xia, T. Cao, W. Bao, C. Wang, and Y. Wang, Discovery of intrinsic ferromagnetism in two-dimensional van der Waals crystals, Nature (London) **546**, 265 (2017).

[24] Y. Deng, Y. Yu, Y. Song, J. Zhang, N. Z. Wang, Z. Sun, Y. Yi, Y. Z. Wu, S. Wu, and J. Zhu, Gate-tunable room-temperature ferromagnetism in two-dimensional Fe_3GeTe_3, Nature (London) **563**, 94 (2018).

[25] M. Bonilla, S. Kolekar, Y. Ma, H. C. Diaz, V. Kalappattil, R. Das, T. Eggers, H. R. Gutierrez, M.-H. Phan, and M. Batzill, Strong room-temperature ferromagnetism in VSe_2 monolayers on van der Waals substrates, Nat. Nanotechnol. **13**, 289 (2018).

[26] J. Liang, W. Wang, H. Du, A. Hallal, K. Garcia, M. Chshiev, A. Fert, and H. Yang, Very large Dzyaloshinskii-Moriya interaction in two-dimensional Janus manganese dichalcogenides and its application to realize skyrmion states, Phys. Rev. B **101**, 184401 (2020).

[27] Q. Cui, J. Liang, Z. Shao, P. Cui, and H. Yang, Strain-tunable ferromagnetism and chiral spin textures in two-dimensional Janus chromium dichalcogenides, Phys. Rev. B **102**, 094425 (2020).

[28] C. Xu, J. Feng, S. Prokhorenko, Y. Nahas, H. Xiang, and L. Bellaiche, Topological spin texture in Janus monolayers of the chromium trihalides $Cr(I, X)_3$, Phys. Rev. B **101**, 060404(R) (2020).

[29] Y. Zhang, C. Xu, P. Chen, Y. Nahas, S. Prokhorenko, and L. Bellaiche, Emergence of skyrmionium in a two-dimensional $CrGe(Se, Te)_3$ Janus monolayer, Phys. Rev. B **102**, 241107(R) (2020).

[30] W. Sun, W. Wang, H. Li, G. Zhang, D. Chen, J. Wang, and Z. Cheng, Controlling bimerons as skyrmion analogues by ferroelectric polarization in 2D van Der Waals multiferroic heterostructures, Nat. Commun. **11**, 5930 (2020).

[31] T.-E. Park, L. Peng, J. Liang, A. Hallal, F. S. Yasin, X. Zhang, K. M. Song, S. J. Kim, K. Kim, M. Weigand, G. Schütz, S. Finizio, J. Raabe, K. Garcia, J. Xia, Y. Zhou, M. Ezawa, X. Liu, J. Chang, H. C. Koo *et al.*, Néel-Type skyrmions and their current-induced motion in van Der Waals ferromagnet-based heterostructures, Phys. Rev. B **103**, 104410 (2021).

[32] Y. Wu, S. Zhang, J. Zhang, W. Wang, Y. L. Zhu, J. Hu, G. Yin, K. Wong, C. Fang, C. Wan, X. Han, Q. Shao, T. Taniguchi, K. Watanabe, J. Zang, Z. Mao, X. Zhang, and K. L. Wang, Néel-type skyrmion in WTe_2/Fe_3GeTe_2 van Der Waals heterostructure, Nat. Commun. **11**, 3860 (2020).

[33] G. Chen, A. Mascaraque, H. Jia, B. Zimmermann, M. Robertson, R. L. Conte, M. Hoffmann, M. A. González Barrio, H. Ding, R. Wiesendanger, E. G. Michel, S. Blügel, A. K. Schmid, and K. Liu, Large Dzyaloshinskii-Moriya interaction induced by chemisorbed oxygen on a ferromagnet surface, Sci. Adv. **6**, eaba4924 (2020).

[34] J. Liang, Q. Cui, and H. Yang, Electrically switchable Rashba-type Dzyaloshinskii-Moriya interaction and skyrmion in two-dimensional magnetoelectric multiferroics, Phys. Rev. B **102**, 220409(R) (2020).

[35] Q. Cui, Y. Zhu, J. Jiang, J. Liang, D. Yu, P. Cui, and H. Yang, Ferroelectrically controlled topological magnetic phase in a Janus-magnet-based multiferroic heterostructure, Phys. Rev. Research **3**, 043011 (2021).

[36] B. van Laar and D. Ijdo, Preparation, crystal structure, and magnetic structure of $LiCrS_2$ and $LiVS_2$, J. Solid State Chem. **3**, 590 (1971).

[37] F. Engelsman, G. Wiegers, F. Jellinek, and B. Van Laar, Crystal structures and magnetic structures of some metal (I) chromium (III) sulfides and selenides, J. Solid State Chem. **6**, 574 (1973).

[38] S. Kobayashi, H. Ueda, C. Michioka, and K. Yoshimura, Competition between the direct exchange interaction and superexchange interaction in layered compounds $LiCrSe_2$, $LiCrTe_2$, and $NaCrTe_2$ with a triangular lattice, Inorg. Chem. **55**, 7407 (2016).

[39] J. Wang, J. Deng, X. Liang, G. Gao, T. Ying, S. Tian, H. Lei, Y. Song, X. Chen, J. Guo, and X. Chen, Spin-flip-driven giant magnetotransport in A-type antiferromagnet $NaCrTe_2$, Phys. Rev. Materials **5**, L091401 (2021).

[40] W. Xu, S. Ali, Y. Jin, X. Wu, and H. Xu, Intrinsic ferromagnetic semiconductors in two-dimensional alkali-based chromium chalcogenides, ACS Appl. Electron. Mater. **2**, 3853 (2020).

[41] S. J. R. Tan, I. Abdelwahab, Z. Ding, X. Zhao, T. Yang, G. Z. J. Loke, H. Lin, I. Verzhbitskiy, S. M. Poh, H. Xu, C. T. Nai, W. Zhou, G. Eda, B. Jia, and K. P. Loh, Chemical stabilization of 1T′, phase transition metal dichalcogenides with giant optical Kerr nonlinearity, J. Am. Chem. Soc. **139**, 2504 (2017).

[42] Z. Shadike, Y.-N. Zhou, L.-L. Chen, Q. Wu, J.-L. Yue, N. Zhang, X.-Q. Yang, L. Gu, X.-S. Liu, S.-Q. Shi, and Z.-W. Fu, Antisite occupation induced single anionic redox chemistry and structural stabilization of layered sodium chromium sulfide, Nat. Commun. **8**, 566 (2017).

[43] Y. Chen, W. Xing, X. Wang, B. Shen, W. Yuan, T. Su, Y. Ma, Y. Yao, J. Zhong, Y. Yun, X. C. Xie, S. Jia, and W. Han, Role of oxygen in ionic liquid gating on two-dimensional $Cr_2Ge_2Te_6$: A non-oxide material, ACS Appl. Mater. Interfaces **10**, 1383 (2018).

[44] I. A. Verzhbitskiy, H. Kurebayashi, H. Cheng, J. Zhou, S. Khan, Y. P. Feng, and G. Eda, Controlling the magnetic anisotropy in $Cr_2Ge_2Te_6$ by electrostatic gating, Nat. Electron. **3**, 460 (2020).

[45] C. Huang, J. Guan, Q. Li, F. Wu, P. Jena, and E. Kan, Built-in electric field control of magnetic coupling in van Der Waals semiconductors, Phys. Rev. B **103**, L140410 (2021).

[46] L. Herrera Diez, Y. T. Liu, D. A. Gilbert, M. Belmeguenai, J. Vogel, S. Pizzini, E. Martinez, A. Lamperti, J. B. Mohammedi, A. Laborieux, Y. Roussigne, A. J. Grutter, E. Arenholtz, P. Quarterman, B. Maranville, S. Ono, M. S. E. Hadri, R. Tolley, E. E. Fullerton, L. Sanchez-Tejerina, A. Stashkevich *et al.*, Nonvolatile Ionic Modification of the Dzyaloshinskii-Moriya Interaction, Phys. Rev. Applied **12**, 034005 (2019).

[47] G. Kresse and J. Hafner, Ab initio molecular dynamics for liquid metals, Phys. Rev. B **47**, 558 (1993).

[48] G. Kresse and J. Furthmüller, Efficient iterative schemes for ab initio total-energy calculations using a plane-wave basis set, Phys. Rev. B **54**, 11169 (1996).

[49] G. Kresse and J. Furthmüller, Efficiency of ab-initio total energy calculations for metals and semiconductors using a plane-wave basis set, Comput. Mater. Sci. **6**, 15 (1996).

[50] Y. Wang and J. P. Perdew, Correlation hole of the spin-polarized electron gas, with exact small-wave-vector and high-density scaling, Phys. Rev. B **44**, 13298 (1991).

[51] G. Kresse and D. Joubert, From Ultrasoft Pseudopotentials to the Projector Augmented-Wave Method, Phys. Rev. B **59**, 1758 (1999).

[52] N. Marom, A. Tkatchenko, M. Rossi, V. V. Gobre, O. Hod, M. Scheffler, and L. Kronik, Dispersion interactions with density-functional theory: Benchmarking semiempirical and interatomic pairwise corrected density functionals, J. Chem. Theory Comput. **7**, 3944 (2011).

[53] See Supplemental Material at http://link.aps.org/supplemental/10.1103/PhysRevB.106.024419 for (1) the SOC included spiral energy dispersion and DMI energy rotating in the *x*-*z* plane for all the $ACrX_2$ monolayers; (2) the comparison of lattice parameters from bulk counterparts, previous works, and this work for $ACrX_2$; (3) the influence of U_{eff} values to magnetic parameters; (4) the SOC included spiral energy dispersion and DMI energy rotating in the *x*-*y* plane for $ACrX_2$ monolayers; (5) computational details of determining NN, NNN, NNNN Heisenberg exchange couplings; (6) comptational details of determining the biquadratic interaction for $LiCrTe_2$ monolayer; and (7) spin textures for $ACrX_2$ monolayers obtained from atomistic simulations.

[54] G. Daalderop, P. Kelly, and M. Schuurmans, First-principles calculation of the magnetocrystalline anisotropy energy of iron, cobalt, and nickel, Phys. Rev. B **41**, 11919 (1990).

[55] A. Hallal, H. X. Yang, B. Dieny, and M. Chshiev, Anatomy of perpendicular magnetic anisotropy in Fe/MgO magnetic tunnel junctions: First-principles insight, Phys. Rev. B **88**, 184423 (2013).

[56] M. Heide, G. Bihlmayer, and S. Blügel, Describing Dzyaloshinskii-Moriya spirals from first principles, Phys. B: Condens. Matter **404**, 2678 (2009).

[57] L. M. Sandratskii, Insight into the Dzyaloshinskii-Moriya interaction through first-principles study of chiral magnetic structures, Phys. Rev. B **96**, 024450 (2017).

[58] B. Zimmermann, G. Bihlmayer, M. Böttcher, M. Bouhassoune, S. Lounis, J. Sinova, S. Heinze, S. Blügel, and B. Dupé, Comparison of first-principles methods to extract magnetic parameters in ultrathin films: Co/Pt(111), Phys. Rev. B **99**, 214426 (2019).

[59] H. Yang, O. Boulle, V. Cros, A. Fert, and M. Chshiev, Controlling Dzyaloshinskii-Moriya interaction via chirality dependent atomic-layer stacking, insulator capping and electric field, Sci. Rep. **8**, 12356 (2018).

[60] M. Heide, G. Bihlmayer, and S. Blügel, Dzyaloshinskii-Moriya interaction accounting for the orientation of magnetic domains in ultrathin films: Fe/W(110), Phys. Rev. B **78**, 140403(R) (2008).

[61] P. M. Lévy and A. Fert, Anisotropy induced by nonmagnetic impurities in Cu Mn spin-glass alloys, Phys. Rev. B **23**, 4667 (1981).

[62] E. Y. Vedmedenko, P. Riego, J. A. Arregi, and A. Berger, Interlayer Dzyaloshinskii-Moriya Interactions, Phys. Rev. Lett. **122**, 257202 (2019).

[63] Q. Zhang, J. Liang, K. Bi, L. Zhao, H. Bai, Q. Cui, H. Zhou, H. Bai. H. Feng, H. Feng, W. Song, G. Chai, O. Gladii, H. Schultheiss, T. Zhu, J. Zhang, Y. Peng, H. X. Yang, and W. Jiang, Quantifying the Dzyaloshinskii-Moriya Interaction Induced by the Bulk Magnetic Asymmetry, Phys. Rev. Lett. **128**, 167202 (2022).

[64] G. Henkelman, A. Arnaldsson, and H. Jónsson, A fast and robust algorithm for Bader decomposition of charge density, Comput. Mater. Sci. **36**, 354 (2006)

[65] E. Sanville, S. D. Kenny, R. Smith, and G. Henkelman, Improved grid-based algorithm for Bader charge allocation, J. Comput. Chem. **28**, 899 (2007)

[66] W. Tang, E. Sanville, and G. Henkelman, A grid-based Bader analysis algorithm without lattice bias, J. Phys.: Condens. Matter **21**, 084204 (2009).

[67] M. Yu and D. R. Trinkle, Accurate and efficient algorithm for Bader charge integration, J. Chem. Phys. **134**, 064111 (2011).

[68] A. Belabbes, G. Bihlmayer, F. Bechstedt, S. Blügel, and A. Manchon, Hund's rule-Driven Dzyaloshinskii-Moriya Interaction at 3d-5d Interfaces, Phys. Rev. Lett. **117**, 247202 (2016).

[69] H. Jia, B. Zimmermann, G. Michalicek, G. Bihlmayer, and S. Blügel, Electric dipole moment as descriptor for interfacial Dzyaloshinskii-Moriya interaction, Phys. Rev. Materials **4**, 024405 (2020).

[70] B. Yang, Q. Cui, J. Liang, M. Chshiev, and H. Yang, Reversible control of Dzyaloshinskii-Moriya interaction at the graphene/co interface via hydrogen absorption, Phys. Rev. B **101**, 014406 (2020).

[71] J. Xiao, D. Legut, W. Luo, H. Guo, X. Liu, R. Zhang, and Q. Zhang, Modulating superexchange strength to achieve robust ferromagnetic couplings in two-dimensional semiconductors, Phys. Rev. B **101**, 014431 (2020).

[72] G. Beutier, S. P. Collins, O. V. Dimitrova, V. E. Dmitrienko, M. I. Katsnelson, Y. O. Kvashnin, A. I. Lichtenstein, V. V. Mazurenko, A. G. A. Nisbet, E. N. Ovchinnikova, and D. Pincini, Band Filling Control of the Dzyaloshinskii-Moriya Interaction in Weakly Ferromagnetic Insulators, Phys. Rev. Lett. **119**, 167201 (2017).

[73] H.-B. Luo, H.-B. Zhang, and J. P. Liu, Strong hopping induced Dzyaloshinskii-Moriya interaction and skyrmions in elemental cobalt, npj Comput. Mater. **5**, 50 (2019).

[74] F. Xue, Z. Wang, Y. Hou, L. Gu, and R. Wu, Control of magnetic properties of $MnBi_2Te_4$ using a van Der Waals ferroelectric $III_2 - VI_3$ film and biaxial strain, Phys. Rev. B **101**, 184426 (2020).

[75] S. Paul, S. Haldar, S. von Malottki, and S. Heinze, Role of higher-order exchange interactions for skyrmion stability, Nat. Commun. **11**, 4756 (2020).

[76] M. J. Freiser, Thermal variation of the pitch of helical spin configurations, Phys. Rev. **123**, 2003 (1961).

[77] J. Y. Ni, X. Y. Li, D. Amoroso, X. He, J. S. Feng, E. J. Kan, S. Picozzi, and H. J. Xiang, Giant Biquadratic Exchange in 2D Magnets and Its Role in Stabilizing Ferromagnetism of $NiCl_2$ Monolayers, Phys. Rev. Lett. **127**, 247204 (2021).

[78] M. Hoffmann and S. Blügel, Systematic derivation of realistic spin models for beyond-Heisenberg solids, Phys. Rev. B **101**, 024418 (2020).

[79] P. B. Ndiaye, A. Abbout, V. M. L. D. P. Goli, and A. Manchon, Quantum anomalous Hall effect and Anderson-Chern insulating regime in the noncollinear antiferromagnetic 3Q state, Phys. Rev. B **100**, 144440 (2019).

[80] D. Amoroso, P. Barone, and S. Picozzi, Spontaneous skyrmionic lattice from anisotropic symmetric exchange in a Ni-halide monolayer, Nat. Commun. **11**, 5784 (2020).

[81] A. Vansteenkiste, J. Leliaert, M. Dvornik, M. Helsen, F. Garcia-Sanchez, and B. Van Waeyenberge, The design and verification of $MuMax_3$, AIP Adv. **4**, 107133 (2014).

[82] M. Heigl, S. Koraltan, M. Vaňatka, R. Kraft, C. Abert, C. Vogler, A. Semisalova, P. Che, A. Ullrich, T. Schmidt, J. Hintermayr, D. Grundler, M. Farle, M. Urbánek, D. Suess, and M. Albrecht, Dipolar-stabilized first and second-order antiskyrmions in ferrimagnetic multilayers, Nat. Commun. **12**, 2611 (2021).

[83] A. Bernand-Mantel, C. B. Muratov, and T. M. Simon, Unraveling the role of dipolar versus Dzyaloshinskii-Moriya interactions in stabilizing compact magnetic skyrmions, Phys. Rev. B **101**, 045416 (2020).

[84] R. F. Evans, W. J. Fan, P. Chureemart, T. A. Ostler, M. O. Ellis, and R. W. Chantrell, Atomistic spin model simulations of magnetic nanomaterials, J. Phys.: Condens. Matter **26**, 103202 (2014).